pp. 1–18 (2016)

Modelling of the electric field distribution in the brain during tDCS

A. V. Ashikhmin* and R. R. Aliev*†

Abstract — We simulated the electric current distribution in the brain during transcranial direct current stimulation (tDCS) using an anatomically accurate human head model. We estimated an effect of common electrode montages on spatial distribution of the electric field during tDCS procedure and analyzed a sensitivity of the technique to variations of electrode size and orientation. We concluded that the used electrode montages are stable with respect to minor changes in electrode size and position, while an assumption of homogeneity and isotropy of the head model results in crucial changes of the electric field distribution. We determined the electrode montages suited to deliver strong effect on hippocampus and cerebellum.

Keywords: Transcranial direct current stimulation, finite element method, anatomical human head model, electric field distribution, computational modelling.

MSC 2010: 65N30, 65N50, 92C02, 92C20, 92C50

Transcranial direct current stimulation (tDCS) is a noninvasive technique for human brain stimulation, which uses weak current delivered via electrodes on the scalp. The technique allows to control intracranial current flow to alter neuronal activity and behaviour [26] by depressing neuronal excitability during cathodal stimulation (hyperpolarization) or facilitating excitations during anodal stimulation (depolarization) [28]. Interest to tDCS has been growing over the last decades as the method can be utilized for numerous therapeutic and research purposes. Considering the variety of electrodes positions on the scalp, transcranial stimulation gives a wide range of possible applications, including treatment of psychiatric and neurological disorders such as depression [25], Parkinson's disease [5], epilepsy [27], as well as improvement of executive functions [15], motor and cognitive activities [26].

Measuring of current induced through the scalp either *in vivo* or *in vitro* experiment is a challenging study. Thus, an estimation of the electric field distribution within the volume of human head and brain requires extensive numerical computations. The range of earlier implemented computational models spreads from simplified geometries of head and electrodes [22] (concentric spheres and points, respectively) to complex multi-layered meshes, taking into account tissue anisotropy

*Laboratory of Human Physiology, Moscow Institute of Physics and Technology, Dolgoprudny 141700, Moscow region, Russia. E-mail: clegling@gmail.com

†Institute of Theoretical and Experimental Biophysics of the RAS. Pushchino, Moscow region 142290, Russia. Federal Medical–Biological Agency, Moscow 123182, Russia

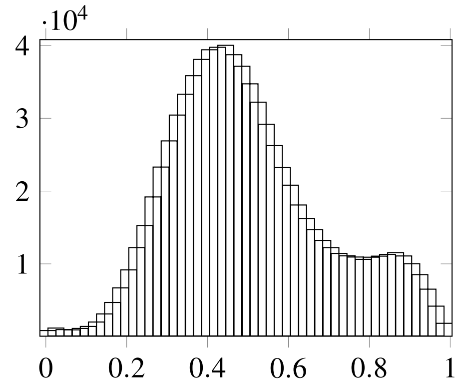

Figure 1. Mesh elements quality histogram.

Table 1.
The mesh statistics.

Mesh statistics parameter	Value
Number of tetrahedral elements	1.67×10^6
Number of triangular elements	5.4×10^5
Mesh volume	3.06 L
Average growth rate	3.48
Growth rate standard deviation	2.51
Average element quality	0.5
Element quality standard deviation	0.19

and heterogeneity [2, 31], as well as various electrode systems [6, 7]. Recent studies have used grey-scaled MR images to generate brain and head models [2, 31].

In the present paper we present the results of computer simulations carried out on a computer model that has been created using raw experimental data. The model includes an accurate representation of major internal structures, brain cortex, white and grey matter from a segmented whole-head MR data set. In comparison with other studies, our model has a neat mesh with the same number of basis elements. Thus, it required less computational resources, while meeting the requirements for the same detalization of the tissues. Appropriate conductivity values as well as anisotropy (conductivity tensor) were applied to all tissues. Electrodes of various sizes and shapes typically used in tDCS experiments were modelled as saline-soaked sponges. The main objectives of this research were: (a) to calculate the electric field distribution across three electrode montages typical for neurology studies; (b) to perform a sensitivity analysis determining the role of applied tissue heterogeneity and anisotropy; (c) to estimate an effect of size and orientation of electrodes on intracranial current flow; (d) to calculate the electric field intensity across major deep brain structures as well as parts of brain cortex, such as primary motor, visual, somatosensory and dorsolateral prefrontal cortex.

1. Methods

1.1. Model

A realistic human head model was reconstructed from MRI scans (woman, 23 years). Anonymized data were retrieved from the NIH functional connectomes repository. To segment these images with 1 mm resolution we used BrainSuite (version 14b1) for head and skull tissues [8, 33] and Harvard FreeSurfer (version 5.3.0) for CSF, white and grey matter [14] and for subcortical neuroanatomical structures [13]. Finally, electrodes were introduced to the model and finite element mesh was generated, using an open-source surface and volumetric mesh generator iso2mesh [9]. This software allows us to control mesh density in the separate parts and regions. To prevent intersections between adjacent surfaces and to eliminate volume defects, all the surfaces were converted into binary images that were subjected to additional correction. As a result we obtained multilayer head and brain geometry that included white and grey matter, cerebrospinal fluid, compact and spongy bones of the skull, and scalp. The realistic head model consisted of 1.67×10^6 tetrahedrons with average edge length of 2.7 mm and standard deviation of 1.6 mm. Quality of the generated mesh was estimated using Joe–Liu mesh quality metrics [21]. Figure 1 presents the quality metric distribution for all tetrahedrons of the whole head model. Additional mesh statistics parameters are in Table 1, where growth rate is the difference in size of two adjacent mesh elements.

1.2. Electrodes

To simulate typical tDCS procedures we considered a bipolar system of electrodes including an anode (positive) and a cathode (negative). As the montages of the electrodes vary significantly among different transcranial stimulation researches [26], we have chosen four most frequent placements and three configurations: each electrode was represented as 5×7 cm^2 rectangular sponge, 5×5 cm^2 square pad and 5×3 cm^2 smaller rectangular electrode. The design of the electrodes is typical for a transcranial stimulation set-up. To simulate realistic experimental conditions, we assumed that the pads did not have an ideal contact with the skin: a gap between the sponge and the scalp was filled with an electrode gel (a highly conductive medium).

Electrode placements for a 5×7 cm^2 rectangular pad configuration are shown in Fig. 2 and described as follows (positions are given in accordance with the commonly used in neurophysiology 10–20 system of markers, where the actual distances between adjacent electrodes are either 10% or 20% of the total front–back or right–left distance of the skull [20]):

(a) The anode was placed over F7-FT7 marks of the 10–20 system with the upper edge of the pad 1.5 cm above the eye socket and the long axis parallel to the horizontal line. The cathode was placed over right mastoid around P8-TP8 with the long axis parallel to the vertical line.

(b) The anode was placed over primary somatosensory cortex around Cz-CPz

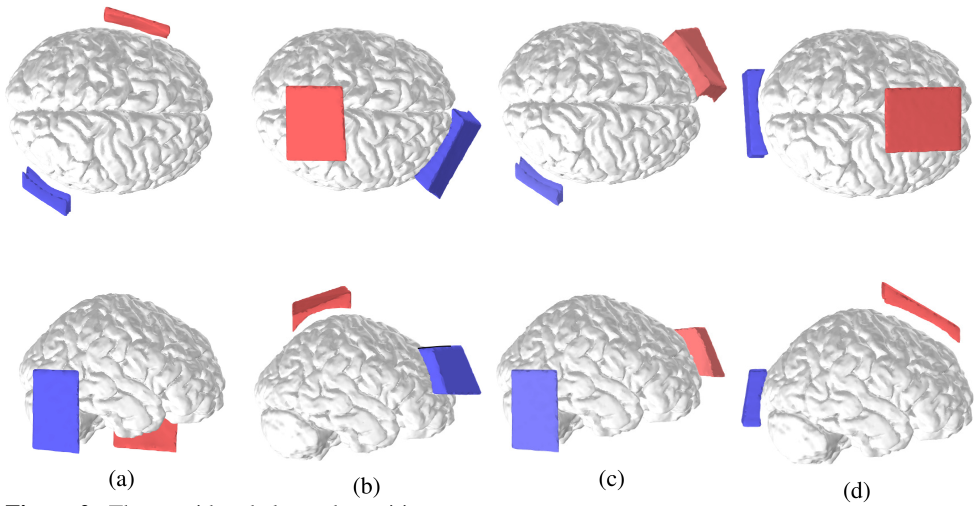

Figure 2. The considered electrode positions.

EEG cap markers. The cathode was placed above the arcus superciliaris on the right with the long axis of the rectangular pad parallel to the horizontal line.

(c) The anode was placed above the arcus superciliaris on the left with the long axis of the rectangular pad parallel to the horizontal line. The cathode was placed over right mastoid around P8-TP8 EEG cap electrode side with the long axis parallel to the vertical line.

(d) The anode was placed over gigantopiramidal, agranular and intermediate frontal zones around Fz electrode side with the long axis parallel to the sagittal plane. The cathode was placed over the occipital lobe around Oz marker with the long axis parallel to the horizontal line.

1.3. Conductivities

Each layer of the model was assumed to be electrically homogeneous and isotropic, except for white matter whose anisotropy is specified in the following paragraph. The tissue conductivities represent the average values (Table 2) taken from experimental studies [1–3, 16, 18, 19, 29, 31, 32, 34]; the value for electrode saline-soaked sponge was estimated for a saline solution for concentration of 100 mM; the value for electrode gel conductivity was taken from manufacturers data. The studies [32, 34] have shown that white matter anisotropy leads to significant deviation in the local electric field value. Numerical modelling and experimental data have demonstrated that longitudinal conductivity is ten times higher than the transverse conductivity of white matter [24, 32, 35]. All these facts were incorporated into the current model.

Table 2.
The tissue conductivities.

Tissue type or compartment	Electrical conductivity value (S/m)
Scalp (skin and fat)	0.41 [19]
Skull (spongy bone)	0.028 [1]
Skull (compact bone)	0.006 [1]
Skull tissues (average value)	0.015 [29]
CSF	1.79 [3]
Grey matter	0.31 [16]
White matter (average)	0.15 [16,24]
White matter (longitudinal)	0.65 [16,24]
White matter (transverse)	0.065 [16,24]
Electrode saline-soaked sponge (100 mM)	1.4
Electrode gel	2.5

1.4. Current distribution model

In this study each layer of the head and brain as well as other parts of the model were assumed as passive conductors. To simulate the current distribution we solved a Laplace equation for the electric potential with the following boundary conditions on the electrodes:

$$\begin{aligned} &\nabla\cdot(-\sigma\nabla\varphi) = 0 \ \text{ in } \Omega \\ &j_n = 0 \ \text{ in } \partial\Omega\backslash S \\ &\begin{cases} \varphi = \pm V & \text{in } S \\ \iint\limits_S j_n\,\mathrm{d}s = I \end{cases} \end{aligned} \tag{1.1}$$

where φ is the electric potential, j_n is a normal component of the electric current density, σ is the conductivity tensor, S is the electrode area, the current I was set to 1.5 mA.

Consequently, the current density for 5×7 cm^2 rectangular pad electrodes was approximately ± 0.4 A/m^2. For test simulations we use the direct solver with constant positive voltage $+V$ applied to the anode and negative voltage $-V$ applied to the cathode. Then we check the boundary condition for normal component of the electric current density as in (1.1) using data from the solution. We continue to vary the applied voltage in the model until condition (1.1) will be fulfilled as the actual tDCS device realizes during the procedure. This voltage is considered as a true voltage that provides both required total current value injected through the scalp and a uniform potential distribution in the electrodes area of the scalp. The following restrictions were also applied to the model: continuity of the normal component of current density on all internal surfaces; zero normal component of current density on external surface (electrical insulation).

The electric field at all nodes of the mesh was calculated as the gradient of the electric potential and the current density in tissues was obtained as product of the electric field value and the electrical conductivity of the related brain tissue:

$$E = \nabla\varphi, \qquad j = \sigma E.$$

For the sensitivity analysis electric field was calculated for the Fz-Oz electrode placement (see Fig. 2d) to check the influence of tissue heterogeneity and anisotropy as well as the effect of electrode size and orientation. In order to analyze the influence of electrode size, the anode was replaced with 5×5 cm^2 and 5×3 cm^2 smaller ones with the same centering; to analyze the influence of electrode orientation anode was turned by 90 degrees and then the average effect was calculated as the absolute and relative differences in maximum and average electric field value.

To estimate the electric potential distribution we used finite element numerical solver COMSOL Multiphysics (version 5.0). It implements both a conjugate gradient method and an iterative solver (GMRES) with incomplete LU factorization as a preconditioner. Calculations were performed on a workstation with 2 GHz Intel Core i7-3667U and 16 GB 1600 MHz RAM running on OS X 10.10. Since the tolerance of potential measurements in neurons is of the order of microvolts and typical value of extracellular potential in the brain is of the order of millivolts, a direct solver for the stationary equations was set to 10^{-3} relative error tolerance. So it took about 5 min for each simulation with approximately 2.2×10^6 degrees of freedom.

2. Results

2.1. Effects of tissue heterogeneity

To study the effect of tissue heterogeneity, we applied four different sets of conductivity values to all tissues of the head model as it was proposed in [6, 23]. The changes were implemented to the Fz-Oz electrode configuration (see Fig. 2d), where conductivity of electrodes and scalp has been set to the original values (Table 2). In the first set white and grey matter conductivities were changed to $\sigma_0 = 0.41$ S/m (average conductivity of the head [16, 19]). Then the following variations of conductivities from Table 2 were applied: in the second set conductivity of cerebrospinal fluid was changed to σ_0; in the third set conductivity of skull was changed to σ_0; in the last set conductivities of all tissues were changed to σ_0, i.e., isotropic and homogeneous head model.

Figure 3 presents the distributions of electric field on the brain cortex for different conductivity sets. In particular, it demonstrates that in the inhomogeneous model there is a shift of the maximum magnitude of the field from gyri to sulci. The effect is seen as a shift of colour spectrum to the red side in sulci and to the blue side in gyri (see Fig. 3). Estimations of the maximum and the average magnitude of electric field in the brain for different conductivity sets are shown in Table 3. As a result, an assumption of the head model homogeneity would lead to substantial deviation in estimated quantities: to a ten percent decrease in the value of the maximum electric field magnitude and to an almost twenty percent increase in the value of the average electric field magnitude in comparison with data from the heterogeneous anisotropic head model.

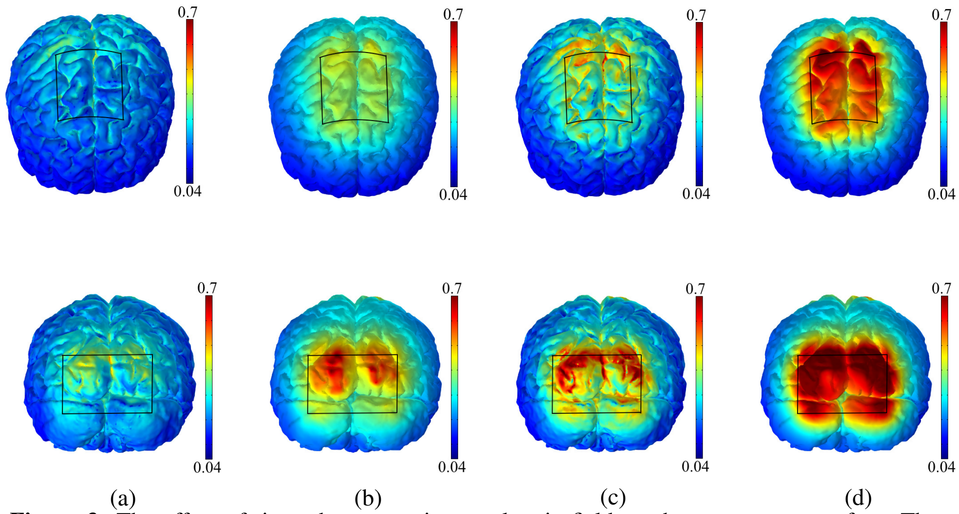

Figure 3. The effect of tissue heterogeneity on electric field on the grey matter surface. The top row shows the distribution near the anode, the bottom row—near the cathode: (a) the isotropic and homogeneous brain model with $\sigma_{\text{scalp}} = \sigma_{\text{WM}} = \sigma_{\text{GM}} = 0.41$ S/m, $\sigma_{\text{CSF}} = 1.79$ S/m, $\sigma_{\text{skull}} = 0.015$ S/m, (b) the model with lower CSF conductivity value $\sigma_{\text{CSF}} = 0.41$ S/m, $\sigma_{\text{skull}} = 0.015$ S/m, (c) the model with higher skull conductivity value $\sigma_{\text{skull}} = 0.41$ S/m, $\sigma_{\text{CSF}} = 1.79$ S/m, (d) the fully isotropic and homogeneous head model with $\sigma = 0.41$ S/m. Color bars scale to V/m.

2.2. Effects of tissue anisotropy

To demonstrate the effect of white matter anisotropy, we simulated a setup with transverse ($\sigma_{yy} = \sigma_{zz} = \sigma_{\text{WM}_{\text{trans}}}$) and longitudinal ($\sigma_{xx} = \sigma_{\text{WM}_{\text{long}}}$) conductivities being assigned to the average value (Table 2) as it was proposed in [7, 23]. A few conductivity sets were tested. In the first conductivity set all the parameters were specified as in the original model. In the second set white matter conductivity was changed to the average value ($\sigma_{xx} = \sigma_{yy} = \sigma_{zz} = \sigma_{\text{WM}_{\text{aver}}}$). Figure 4 illustrates the electric field distribution: particularly, it demonstrates that introduction of the white matter anisotropy to the model significantly changes the form of the electric field under the anode. Table 3 shows the maximum and average electric field magnitude in the brain across different conductivity sets. Comparison of the anisotropic and isotropic heterogeneous model reveals a substantial 20% decrease in the value of average electric field magnitude, while maximum electric field magnitude increased less than 5%.

2.3. Effects of electrode size and orientation

To study the effects of electrode design variations, we have designed three models with typical anode configurations, widely used in clinical tDCS experiments: 5×7 cm^2, 5×5 cm^2 and 3×5 cm^2. Figure 5 demonstrates the electric field distribution for the model with these electrodes: particularly, we observe that the area

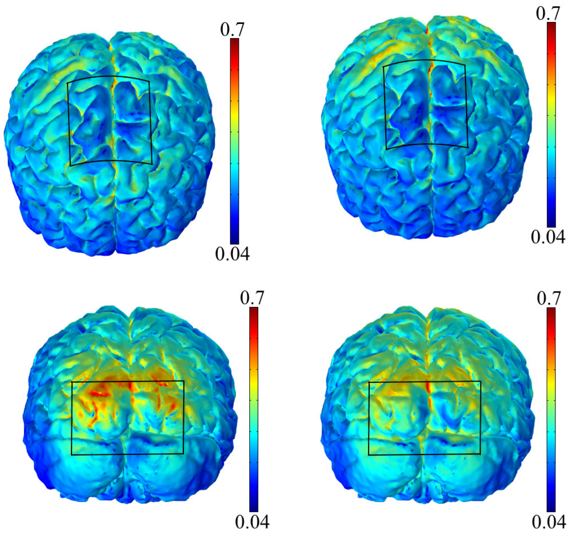

Figure 4. The effect of white matter anisotropy. The top row is the distribution of the electric field magnitude near the anode; the bottom row is the distribution near the cathode. Left and right columns show distributions assuming anisotropic ($\sigma_{\mathrm{WM}_{\mathrm{long}}}$ = 0.65 S/m, $\sigma_{\mathrm{WM}_{\mathrm{trans}}}$ = 0.065 S/m) and isotropic ($\sigma_{\mathrm{WM}_{\mathrm{aver}}}$ = 0.15 S/m) conductivity, respectively. Black rectangles mark the electrodes positions. Color bars scale to V/m.

with the strongest field, invoked by an electrode (yellow spots in the figure), shifts towards the opposite electrode if the electrode size is increased. Table 4 shows numerical characteristics of the simulated field: the maximum and the average electric field magnitude, absolute and relative errors for 5×5 cm^2 and 3×5 cm^2 anodes in comparison with initial 5×7 cm^2 and electrode focality estimation. Particularly, decreasing anode area by 60% (from 5×7 cm^2 to 3×5 cm^2) we obtained 5% growth in the average and 12% growth in the maximum magnitude of the electric field, while the relative difference across the nodes of the brain was about 10%. Despite relatively small changes in the electric field value, there is a strong effect in *focality*. Estimating focality as an area of the cortex with the electric field magnitude higher than 0.3 V/m threshold, we have discovered almost 90% area increase for previously mentioned anode designs (last column in Table 4). An increase of the threshold reduces this area, while the focality effect grows. In case of 0.5 V/m threshold we observed a 0.61 cm^2 area for the 5×7 cm^2 anode and a 1.6 cm^2 area for the 3×5 cm^2 anode resulting in a 163% area increase.

Studying effects of anode orientation, we found slight changes in the electric field distribution (Table 5). Reversing the anode orientation from horizontal to vertical causes less than 1% change in both the maximum and the average electric field value, and less than 2% in relative difference in comparison with the initial anode orientation. In comparison with the previously mentioned effects of tissue inhomogeneity and anisotropy as well as effects of electrode size variation, the change of anode orientation gives much smaller contribution in the electric field alteration.

Table 3.
The effects of tissue heterogeneity and anisotropy. In column σ_{WM}: for anisotropic model two values represent longitudinal ($\sigma_{WM_{long}} = \sigma_{xx}$) and transverse ($\sigma_{WM_{trans}} = \sigma_{yy} = \sigma_{zz}$) components, respectively; for isotropic model one value represents average conductivity ($\sigma_{WM_{aver}} = \sigma_{xx} = \sigma_{yy} = \sigma_{zz}$). The conductivity of the scalp as well as default conductivity value was set to 0.41 S/m.

Conductivity, S/m				Maximum magnitude of electric field, V/m	Average magnitude of electric field, V/m
σ_{skull}	σ_{CSF}	σ_{GM}	σ_{WM}		
0.015	1.79	0.31	0.65	1.036	0.240
0.015	1.79	0.31	0.15	1.094	0.273
0.015	1.79	0.41	0.41	0.737	0.200
0.015	0.41	0.41	0.41	0.685	0.270
0.41	1.79	0.41	0.41	0.938	0.215
0.41	0.41	0.41	0.41	0.913	0.282

Table 4.
The effects of anode size variation. The values for the maximum and average magnitude of the electric field were calculated for the entire brain volume. The errors were estimated relative to the 5×7 cm^2 anode configuration.

Anode size	Maximum magnitude of E-field, V/m	Average magnitude of E-field, V/m	Absolute error, mV/m	Relative error, %	Cortex area with $\lvert E\rvert > 0.3$ V/m, cm^2
5×7	1.036	0.240	—	—	85.1
5×5	1.099	0.250	9.2	3.8	122.4
3×5	1.164	0.252	25.5	10.6	158.6

Table 5.
The effects of electrode orientation. The values for the maximum and average magnitude of the electric field were calculated for the entire brain volume. The errors were estimated in comparison with the results for initial anode orientation.

Anode size	Maximum magnitude of electric field, mV/m	Average magnitude of electric field, mV/m	Absolute error, mV/m	Relative error, %
7×5	1.038	0.241	4.5	1.9
5×3	1.162	0.251	2.1	0.9

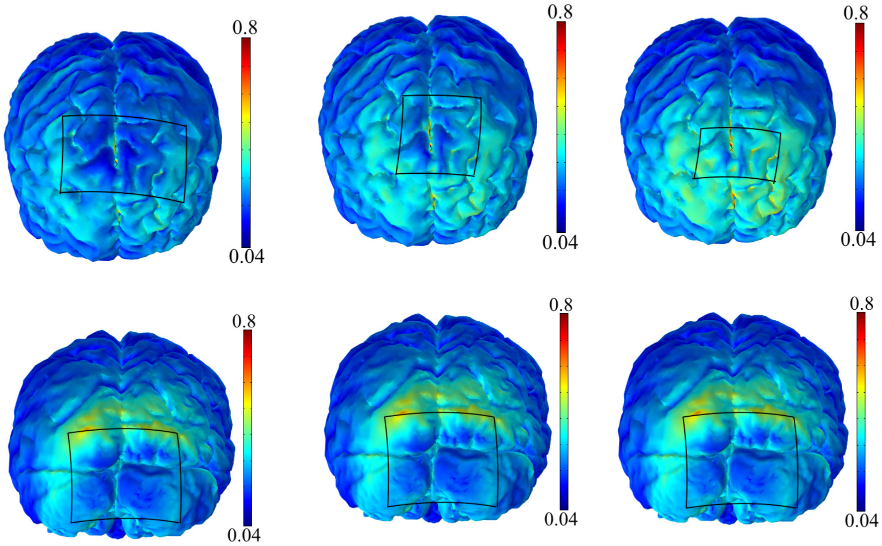

Figure 5. The effect of anode size variation. The top row demonstrates the distribution of the electric field magnitude (in V/m) near the anode; the bottom row shows the distribution near the cathode. Columns from left to right represent the results for three configurations of the anode: 5×7 cm^2, 5×5 cm^2 and 3×5 cm^2. Black rectangles mark the electrodes positions. Color bars scale to V/m.

2.4. Distribution of electric field and effects of electrode placement

The electric field on the cortex surface is shown in Fig. 6. Simulations show that decrease of a distance between the anode and the cathode leads to shifting of the strongest field on gyri from an area under the cathode (see Figs. 6a and 6c) to an area between the anode and the cathode (see Figs. 6b and 6d). Particularly, considering the electrode montage from Fig. 2a we observe the highest electric field magnitude (yellow spots) in the area of the cathode (see Fig. 6a), while for montage from Fig. 2b we observe the highest electric field magnitude (red and yellow spots) in the area between the anode and the cathode (see Fig. 6b). However, the highest values of the electric field magnitude in the whole brain model are buried in the sulci. This statement is also confirmed in Fig. 7 that represents the distribution of the electric field magnitude across different cuts. All these figures illustrate the electric field predominance and current penetration rate both in cortex and in deep brain structures. Therefore, looking through the cuts we can visualize the parts with the strongest electric field.

Simulating electric field and current distribution in the brain, we approach a practical question: Which brain structures can be stimulated with the particular electrodes configuration? To estimate the effect of stimulation we use the average value of spatially distributed magnitude of the electric field. Figure 8 presents a comparison of the effects across deep brain structures and the parts of the cortex. We found that an electrode montage with the anode placed at a greater distance from the cathode (see Figs. 2a and 2c) leads to less shunting, i.e., more electric current reaches

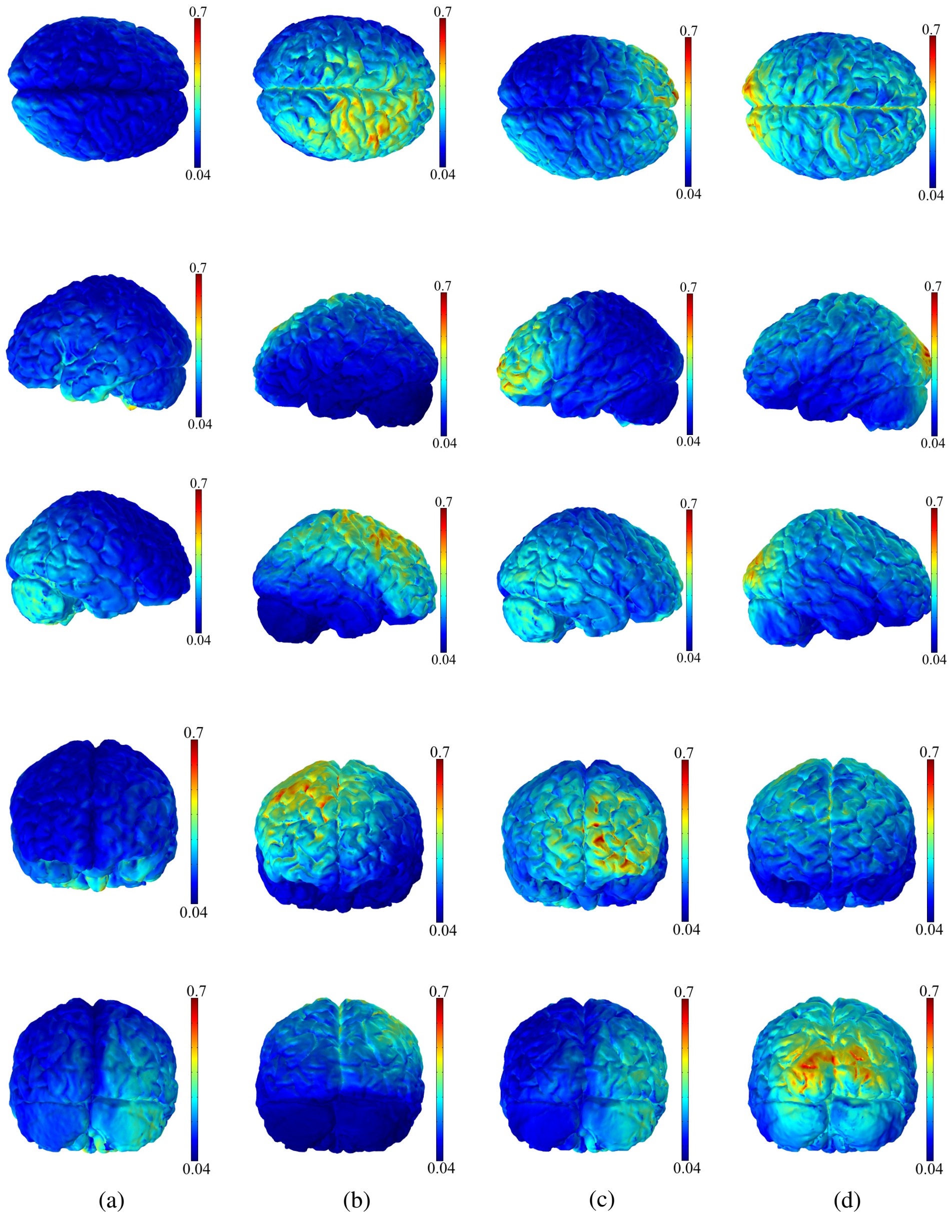

Figure 6. The electric field distribution on the grey matter surface. Each column represents 5×7 cm^2 electrode positions from Fig. 2. Each row stands for views: (1) top, (2) left lateral, (3) right lateral, (4) frontal, (5) posterior view. Color bars scale to V/m.

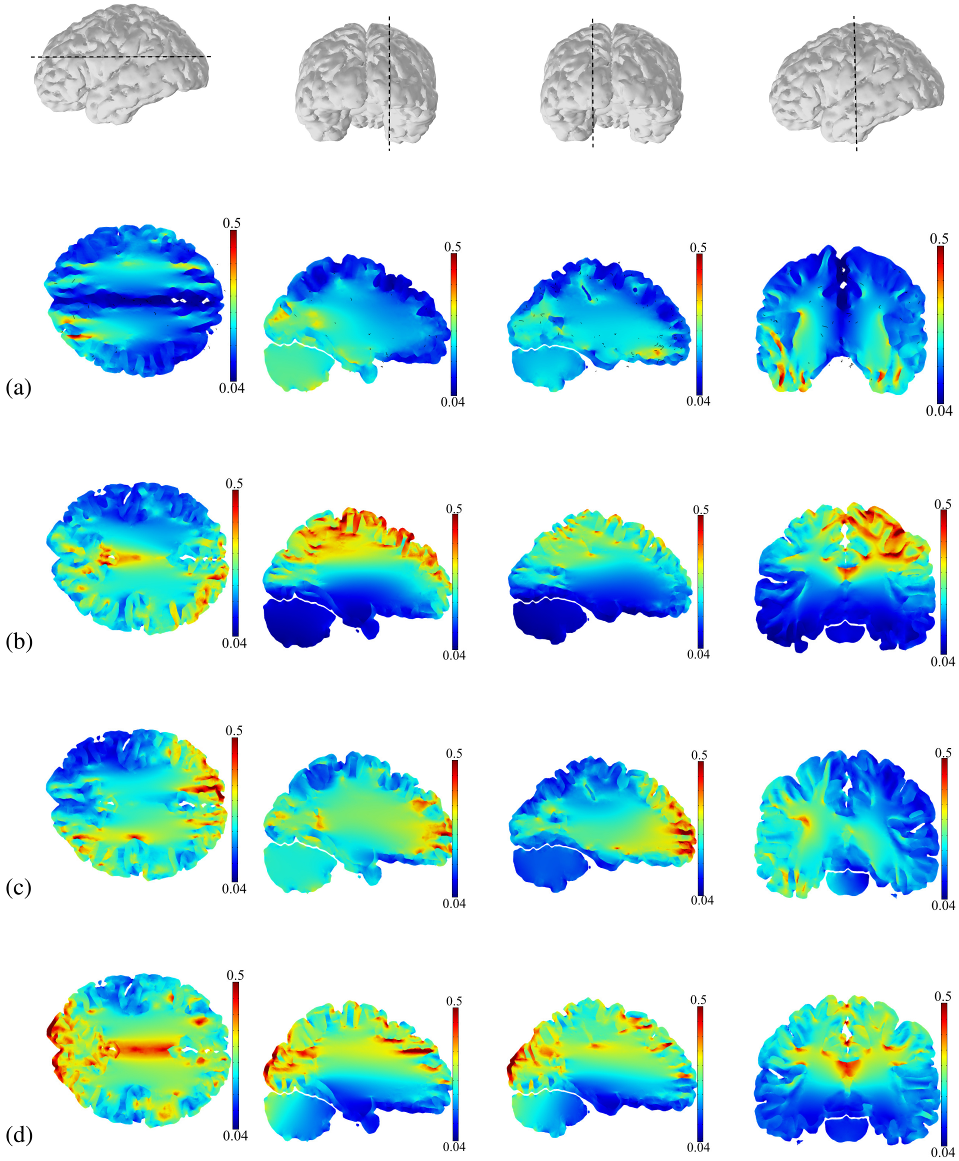

Figure 7. The electric field distribution in cross-sections of the brain. Each column represents a cross-section view as in the very top. Each row represents 5×7 cm^2 electrode positions from Fig. 2. Color bars scale to V/m.

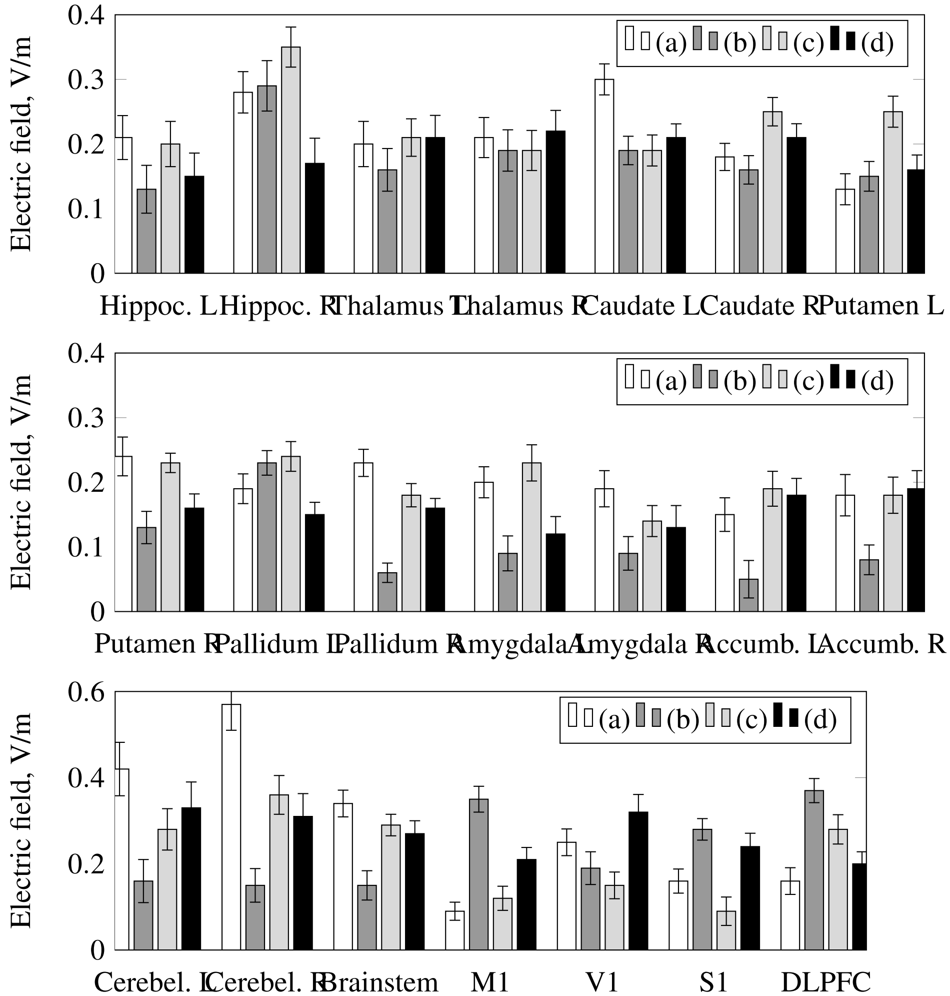

Figure 8. Average magnitude and standard deviation of the electric field in the cortex and in deep brain structures; (a), (b), (c), and (d) are electrode positions from Fig. 2. M1 — primary motor cortex, V1 — primary visual cortex, S1 — primary somatosensory cortex, DLPFC — dorsolateral prefrontal cortex.

the brain. Consequently, the electrode montage from Fig. 2b results in the highest shunting effect. We discovered that the high shunting leads to lower effect on deep brain structures and higher current penetration rate on the cortex. Meanwhile, the other three montages had lower shunting effect, which led to stronger effect on deep brain structures.

3. Discussion

The aim of this paper is threefold: (i) to create a model for accurate simulations of the electric field in the brain; (ii) to study the electric field distributions under different conditions; (iii) to simulate common experimental and clinical set-ups. We tested our model comparing the results of simulations with literature data [2, 6, 7, 22, 23, 30, 31]. In particular, we found that both tissue heterogeneity and anisotropy are important tissue properties which cannot be neglected in realistic simulations. Our study suggests 20% increase in average and 5% reduction in maximum magnitude of the electric field in case of fully homogeneous model with $\sigma = 0.41$ S/m. Reported data [23] show increase of 75% and 25% in average and maximum values, respectively, for model with $\sigma = 0.33$ S/m. Our data are in accordance with the reported results; numeric differences are due to specificity of conductivity tensor as well as non-identical electrodes placement, and head model geometry.

An important part of our work involves simulations of common experimental and clinical tDCS set-ups. We found that replacement of the 5×7 cm^2 anode with a smaller 5×5 cm^2 one led to slight changes in the electric field, while the 3×5 cm^2 anode gave more than 10% difference across the nodes of the brain model in comparison with the 5×7 cm^2 one. Although the changes in the electric field magnitude associated with anode miniaturizing are mild, there is a sufficient alteration in focality (see Fig. 5). Parazzini et al. [30] obtained more than 20% growth in the median electric field amplitude after replacement of the standard 35 cm^2 anode with 10 cm^2 electrode. Meanwhile, Miranda et al. [23] have shown, that changes of anode area lead to weak changes in average electric field magnitude (less than 2.5% for the same anode configurations). However, they also found that the area of the cortex surface where magnitude of the electric field exceeds certain threshold was increasing with decreasing electrode size. Particularly, the cortex surface with the electric field magnitude exceeding 0.15 V/m threshold increased by almost 60% [23]. It was also reported [2] that a displacement of the electrode by 1 cm leads to minor changes in the electric field as well, more significant changes were mentioned in case of the inter-electrode distance reduction, which led to less that 10% change in the electric field magnitude. Consequently, our tDCS modelling shows that electrode orientation and slight displacement lead to minor changes, whereas anode area variation gives much stronger effect in the electric field alteration and focality. The results confirm the data from previous studies.

Although minor changes in the design as well as slight displacements of either anode or cathode lead to insignificant deviations of the electric field in the brain, our simulations demonstrate significant influence of electrode positions both on the cortex and on deep brain structures. An important result of the study is that depending on the montages, we can suggest the effects on particular brain structures. For the electrode positions from Fig. 2a the anode was located over the temporal lobe and the cathode was placed over the left part of the cerebellum. The electrode montage from Fig. 2b represented the anodal stimulation of the primary motor and primary somatosensory cortex and the cathodal stimulation of the right dorsolateral prefrontal cortex. For the electrode positions from Fig. 2c the anode is over the left dorsolateral prefrontal cortex and the cathode is over the left cerebellum. Finally, in the case of Fig. 2d the anodal stimulation was applied over the premotor cortex, while the cathodal stimulation was applied over the primary somatosensory and primary visual cortex. All these assumptions are directly corroborated with the results in Figure 8, which shows corresponding peaks of the electric field magnitude for these structures.

It should be noted that the maximum and average electric field values in the brain are similar to the reported in [6, 7, 22, 23, 30, 31]. For example, we estimate peak cortical value of 1.04 V/m as compared to the literature data ranged from 0.3 to 1.5 V/m. The variations may be due to the differences in the electrode montages, the applied conductivity values and deviations of the head model geometry.

3.1. Clinical application

Our research shows that there is a strong effect of tDCS on the electric field distribution in the cerebellum among placements with cathode located over P8-TP8 or Oz markers (see Fig. 8). Several studies have shown that cerebellum directly involved in motor control and motor learning [10, 12]. Particularly, Ferrucci et al. have reported [10] an improvement in motor skills or cognitive activity after anodal cerebellar tDCS. During the cathodal stimulation over the right part of the cerebellum for the electrode montage from Fig. 2a and 2c, electric current flows in the tangential direction, having the highest rate of electric current induced in this structure (see Figs. 7 and 8). In case of Fig. 2d current mostly spreads in the normal direction, thus having lower penetration rate in comparison with the electrode positions from Figs. 2a and 2c [11]. Moreover, the research has revealed that both anodal and cathodal tDCS over this brain structure blocked the reaction time decrease after repeating the working memory task, being independent of visual system involvement, while Galea et al. [17] has reported the distinct roles for the cerebellum and primary motor cortex during motor learning tasks in anodal tDCS procedure. We did not find link between the current penetration rate in cerebellum and in primary visual and motor cortex as well (see Fig. 8), whereas having the highest electric field intensity in cerebellum for electrode positions from Figs. 2a, 2c and 2d and only slight changes in the electric field intensity between the electrode positions from Figs. 2c and 2d. Therefore, our results are in agreement with the experimental data.

We have also discovered high electric field intensity in hippocampus for a tDCS simulation with the anode located over the parts of the frontal cortex. Clinical trials have reported both antidepressant effects and cognition enhancements that critically linked to the neurogenesis in the dentate gyrus [4]. Fregni et al. have found [15] that anodal tDCS applied over the left dorsolateral prefrontal cortex (see Fig. 2c) enhances accuracy in a three-back letter task in comparison with cathodal stimulation of the same area or anodal stimulation of the primary motor cortex (see Fig. 2b). Our results are in line with these findings for both left and right hippocampus.

The model has limitations due to the following reasons: the original MRI data has a limited coverage, being truncated at the level of C1-C2 cervical vertebrae; the conductivities of all layers were simplified, while the actual tissues of the head have heterogeneous and anisotropic characteristics; the white matter anisotropy was simplified while the actual white matter anisotropy is more complex as retrieved from DT-MRI data; automatic algorithms used for image segmentation and surface generation has a limited accuracy and could not represent the real head model. Nonetheless, employed model has sufficient precision to support the reported results.

References

1. M. Akhtari, H. Bryant, A. Mamelak, E. Flynn, L. Heller, J. Shih, M. Mandelkem, A. Matlachov, D. Ranken, E. Best, M. DiMauro, R. Lee, and W. Sutherling, Conductivities of three-layer live human skull. *Brain Topography* **14** (2002), No. 3, 151–167.
2. S. Bai, S. Dokos, K.-A. Ho, and C. Loo, A computational modelling study of transcranial direct current stimulation montages used in depression. *NeuroImage* **87** (2014), 332–344.
3. S. Baumann, D. Wozny, S. Kelly, and F. Meno, The electrical conductivity of human cerebrospinal fluid at body temperature. *IEEE Trans. Biomed. Engrg.* **44** (1997), No. 3, 220–223.
4. D. Bennabi, S. Pedron, E. Haffen, J. Monnin, Y. Peterschmitt, and V. V. Waes, Transcranial direct current stimulation for memory enhancement: from clinical research to animal models. *Front. Systems Neurosci.* **8** (2014), No. 159, 485–492.
5. D. H. Benninger, M. Lomarev, G. Lopez, E. Wassermann, X. Li, E. Considine, and M. Hallett, Transcranial direct current stimulation for the treatment of Parkinson's disease. *J. Neurology, Neurosurg. Psychiatry* **81** (2010), No. 10, 1105–1111.
6. A. Datta, V. Bansal, J. Diaz, J. Patel, D. Reato, and M. Bikson, Gyri–precise head model of transcranial dc stimulation: Improved spatial focality using a ring electrode versus conventional rectangular pad. *Brain Stimulation* **2** (2009), No. 4, 201–207.
7. A. Datta, M. Elwassif, F. Battaglia, and M. Bikson, Transcranial current stimulation focality using disk and ring electrode configuration: FEM analysis. *J. Neural Engrg.* **5** (2008), 163–174.
8. B. Dogdas, D. Shattuck, and R. Leahy, Segmentation of skull and scalp in 3-d human MRI using mathematical morphology. *Human Brain Mapping* **26** (2005), 273–285.
9. Q. Fang and D. Boas, Tetrahedral mesh generation from volumetric binary and gray-scale images. In: *International Symposium on Biomedical Imaging: From Nano to Macro*. 2009, pp. 1142–1145.
10. R. Ferrucci, A. Brunoni, M. Parazzini, M. Vergari, E. Rossi, M. Fumagalli, F. Mameli, M. Rosa, G. Giannicola, S. Zago, and A. Priori, Modulating human procedural learning by cerebellar transcranial direct current stimulation. *Cerebellum* **12** (2013), No. 4.
11. R. Ferrucci, S. Marceglia, M. Vergari, F. Cogiamanian, S. Mrakic-Sposta, F. Mameli, S. Zago, S. Barbieri, and A. Priori, Cerebellar transcranial direct current stimulation impairs the practice-dependent proficiency increase in working memory. *J. Cognitive Neurosci.* **20** (2008), No. 9, 1687–1697.
12. E. J. Fine, C. C. Ionita, and L. Lohr, The history of the development of the cerebellar examination. *Seminars in Neurology* **22** (2002), No. 4, 375–384.
13. B. Fischl, D. Salat, E. Busa, M. Albert, M. Dieterich, C. Haselgrove, A. van der Kouwe, R. Killiany, D. Kennedy, S. Klaveness, A. Montillo, N. Makris, B. Rosen, and A. Dale, Whole brain segmentation: automated labeling of neuroanatomical structures in the human brain. *Neuron* **33**

(2002), 341–355.

14. B. Fischl, D. Salat, A. van der Kouwe, N. Makris, F. Segonne, B. Quinn, and A. Dalea, Sequence-independent segmentation of magnetic resonance images. *NeuroImage* **23** (2004), S69–S84.
15. F. Fregni, P. Boggio, M. Nitsche, F. Bermpohl, A. Antal, E. Feredoes, M. Marcolin, S. Rigonatti, M. Silva, W. Paulus, and A. Pascual-Leone, Anodal transcranial direct current stimulation of prefrontal cortex enhances working memory. *Experimental Brain Research* **166** (2005), 23–30.
16. C. Gabriel, S. Gabriel, and E. Corthout, The dielectric properties of biological tissues, I: Literature survey. *Physics in Medicine and Biology* **41** (1996), 2231–2249.
17. J. Galea, A. Vazquez, N. Pasricha, J.-J. O. de Xivry, and P. Celnik, Dissociating the roles of the cerebellum and motor cortex during adaptive learning: The motor cortex retains what the cerebellum learns. *Cerebral Cortex* **21** (2011), No. 8, 1761–1770.
18. S. Goncalves, J. Munck, J. Verbunt, F. Bijma, R. Heethaar, and F. L. da Silva, In vivo measurement of the brain and skull resistivities using an eit-based method and realistic models for the head. *IEEE Trans. Biomed. Engrg.* **6** (2003), 754–767.
19. R. N. Holdefer, R. Sadleir, and M. J. Russell, Predicted current densities in the brain during transcranial electrical stimulation. *Clinical Neurophysiol.* **117** (2006), No. 6, 1388–1397.
20. G. Klem, H. Luders, H. Jasper, and C. Elger, The ten-twenty electrode system of the international federation. *Electroencephalography and Clinical Neurophysiol.* **52** (1999), No. 3.
21. A. Liu and B. Joe, Relationship between tetrahedron shape measures. *BIT Numer. Math.* **34** (1994), No. 2, 268–287.
22. P. Miranda, M. Lomarev, and M. Hallett, Modelling the current distribution during transcranial direct current stimulation. *Clinical Neurophysiology* **117** (2006), 1623–1629.
23. P. Miranda, A. Mekonnen, R. Salvador, and G. Ruffini, The electric field in the cortex during transcranial current stimulation. *NeuroImage* **70** (2013), 48–58.
24. P. Nicholson, Specific impedance of cerebral white matter. *Experimental Neurology* **13** (1965), No. 4, 386–401.
25. M. Nitsche, P. Boggio, F. Fregni, and A. Pascual-Leone, Treatment of depression with transcranial direct current stimulation (tDCS): a review. *Experimental Neurology* **219** (2009), 14–19.
26. M. Nitsche, L. Cohen, E. Wassermann, A. Priori, N. Lang, A. Antal, W. Paulus, F. Hummel, P. Boggio, F. Fregni, and A. Pascual-Leone, Transcranial direct current stimulation: state of the art 2008. *Brain Stimulation* **1** (2008), 206–223.
27. M. Nitsche and W. Paulus, Noninvasive brain stimulation protocols in the treatment of epilepsy: current state and perspectives. *Neurotherapeutics* **6**, 244–250.
28. M. Nitsche and W. Paulus, Excitability changes induced in the human motor cortex by weak transcranial direct current stimulation. *J. Physiology* **527** (2000), 633–639.
29. T. Oostendorp, J. Delbeke, and D. Stegeman, The conductivity of the human skull: results of in vivo and in vitro measurements. *IEEE Trans. Biomed. Engrg.* **47** (2000), No. 11, 1487–1492.
30. M. Parazzini, S. Fiocchi, E. Rossi, A. Paglialonga, and P. Ravazzani, Transcranial direct current stimulation: estimation of the electric field and the current density in an anatomical human head model. *IEEE Trans. Biomed. Engrg.* **58** (2011), No. 6, 1773–1780.
31. R. Sadleir, T. Vannorsdall, D.J.Schretlen, and B. Gordon, Transcranial direct current stimulation (tDCS) in a realistic head model. *NeuroImage* **51** (2010), 1310–1318.
32. S. Shahid, P. Wen, and T. T. Ahfock, Numerical investigation of white matter anisotropic conductivity in defining current distribution under tDCS. *Comput. Methods Programs Biomed.* **109** (2013), 48–64.

33. D. Shattuck and R. Leahy, Brainsuite: an automated cortical surface identification tool. *Medical Image Analysis* **6** (2002), 129–142.

34. H. Suh, W. Lee, and T. Kim, Influence of anisotropic conductivity in the skull and white matter on transcranial direct current stimulation via an anatomically realistic finite element head model. *Physics Medicine Biology* **57** (2012), 6961–6980.

35. C. Wolters, A. Anwander, X. Tricoche, D. Weinstein, M. Koch, and R. MacLeod, Influence of tissue conductivity anisotropy on EEG/MEG field and return current computation in a realistic head model: a simulation and visualization study using high-resolution finite element modelling. *NeuroImage* **30** (2006), 813–826.